

MONOGENIC WAVELET SCATTERING NETWORK FOR TEXTURE IMAGE CLASSIFICATION

Wai Ho Chak and Naoki Saito

University of California, Davis
Department of Mathematics
One Shields Avenue, Davis, CA 95616 USA

ABSTRACT

The scattering transform network (STN), which has a similar structure as that of a popular convolutional neural network except its use of predefined convolution filters and a small number of layers, can generate a robust representation of an input signal relative to small deformations. We propose a novel *Monogenic Wavelet Scattering Network* (MWSN) for 2D texture image classification through a cascade of monogenic wavelet filtering with nonlinear modulus and averaging operators by replacing the 2D Morlet wavelet filtering in the standard STN. Our MWSN can extract useful hierarchical and directional features with interpretable coefficients, which can be further compressed by PCA and fed into a classifier. Using the CURET texture image database, we demonstrate the superior performance of our MWSN over the standard STN. This performance improvement can be explained by the natural extension of 1D analyticity to 2D monogenicity.

Index Terms— Scattering Transform, Monogenic Wavelet Transform, Riesz Transform, Texture Image Classification

1. INTRODUCTION

The *scattering transform network* (STN) has an architecture similar to a popular convolutional neural network (CNN). The latter, in particular, its “deep” version called Deep Neural Network (DNN), is known for its ability to extract hierarchical and critical features for many applications such as image classification and facial recognition when large training samples are available [1, 2]. Despite its popularity, the CNN/DNN tends to overfit its model for a dataset of small size. The STN, on the other hand, works well without a gigantic number of examples, and requires no optimization (e.g., stochastic gradients) to learn convolution filters from data since it uses predefined wavelet filters. In addition, the STN typically operates with a small number of layers, say, two or three, which is quite a contrast to the DNN. Yet, Mallat showed that the STN representation of an input signal provides a translation invariant

representation when the scale tends to infinite resolution, and it is Lipschitz continuous under non-uniform translation [3]. Furthermore, Bruna and Mallat demonstrated the power of the STN using image classification examples [4, 5].

A typical software implementation of the STN, e.g., the Kymatio package [6], uses the Morlet wavelet filter as its base wavelet filter. Although the Morlet wavelets are only approximately *analytic* [7], they have been used in the *analytic wavelet transform* (AWT). The AWT provides interpretable multiscale instantaneous magnitude and phase information, which is crucial for 1D signal analysis. When one wants to analyze 2D input images, the concept of analyticity needs to be properly extended: simply considering the tensor product of the 1D AWT would not be sufficient. A properly extended concept of 1D analytic signal to higher dimension is the so-called *monogenic signal* proposed by Felsberg and Sommer [8]; see also [9] for the comprehensive review. Based on the monogenic signal theory, Olhede and Metikas proposed the *monogenic wavelet transform* (MWT) [10] generalizing the 1D AWT. The MWT inherits those desirable properties of AWT for higher-dimensional signals, i.e., provides their multiscale instantaneous magnitude, phase, and orientation information, which would lead to better interpretability of the important features of high-dimensional input signals. Moreover, the isotropic MWT magnitude is invariant to rotations, and its orientation is covariant to rotations [10].

Hence, it is quite natural and in fact inviting to adopt the MWT as the base wavelet transform in the STN framework instead of the 2D Morlet wavelet transform when handling 2D images. By doing so, we can capture 2D geometric features more efficiently than what the Morlet wavelets-based STN could provide.

2. MONOGENIC SIGNALS AND MWT

In this section, after briefly reviewing the concept of an analytic signal and the AWT, we will describe the definition and properties of a monogenic signal and the MWT, which are necessary to discuss our *Monogenic Wavelet Scattering Network* (MWSN) in Section 3.2.

* This research was partially supported by the US National Science Foundation grants DMS-1912747, CCF-1934568; the US Office of Naval Research grant N00014-20-1-2381.

A signal is said to be *analytic* if it is a complex-valued function that has no negative frequency components [11, 12]. The analytic representation provides useful information such as instantaneous amplitude and phase. Hence, if a real-valued signal, say, $g(x) \in L^2(\mathbb{R})$ is given, it is of interest to generate its analytic representation $g^+(x)$ whose real component is $g(x)$. It is well known that its imaginary component can be obtained by the *Hilbert transform* of $g(x)$ [11, 12, 13], i.e.,

$$g^+(x) := g(x) + \mathbf{i}g^{(1)}(x), \quad g^{(1)}(x) := \frac{1}{\pi} \text{p.v.} \int_{-\infty}^{\infty} \frac{g(y)}{x-y} dy,$$

where p.v. means the Cauchy principal value.

The notion of wavelet is also necessary. A *wavelet* (or also known as *mother wavelet*) $\psi(x) \in L^2(\mathbb{R})$ is a function whose translated and dilated versions allow one to perform time-scale/frequency analysis of a signal of interest [14, Chap. 4]. It has to satisfy the *admissibility condition*:

$$\int_{\mathbb{R}} \frac{|\Psi(\xi)|^2}{|\xi|} d\xi < \infty, \quad \int_{\mathbb{R}} |\psi(x)|^2 dx = 1,$$

where $\Psi(\xi)$ is the Fourier transform of $\psi(x)$. In 1D, the *continuous wavelet transform* (CWT) of a signal $g \in L^2(\mathbb{R})$ with respect to the mother wavelet ψ is given by

$$W_{\psi}g(a, b) := \frac{1}{\sqrt{a}} \int_{\mathbb{R}} g(t) \overline{\psi\left(\frac{t-b}{a}\right)} dt,$$

for any $a \in \mathbb{R}_+ := \{x \in \mathbb{R} | x > 0\}$, $b \in \mathbb{R}$. The CWT defines the AWT when ψ is analytic.

We can extend the concept of analyticity to higher dimensions. With the fact that a 1D analytic signal is a boundary value (at the real axis) of a complex-valued analytic function that satisfies the *Cauchy-Riemann equations* in the upper half of the complex plane [13, 9], we can find the analogue of the 2D analytic signal. A popular choice for generalizing the Cauchy-Riemann equations to higher dimensions is *the Riesz system* (of PDEs) [15] in the upper half-space $\mathbb{R}_+^3 := \{\mathbf{x} \in \mathbb{R}^3 | x_3 > 0\}$. Any solution of the Riesz system in \mathbb{R}_+^3 is said to be a *monogenic* [8], and its boundary value at $x_3 = 0$ is called *monogenic signal*.

Next we need to introduce the *quaternion*, which has the form $e := e_0 + e_1\mathbf{i} + e_2\mathbf{j} + e_3\mathbf{k} \in \mathbb{H}$, where \mathbb{H} is the 4D real associative algebra of the quaternions, $\mathbf{i}, \mathbf{j}, \mathbf{k}$ are the quaternion units, and $e_l \in \mathbb{R}$, $l = 0, \dots, 3$. The quaternion units satisfy the following multiplication rules: $\mathbf{i}^2 = \mathbf{j}^2 = \mathbf{k}^2 = -1$; $\mathbf{i}\mathbf{j} = -\mathbf{j}\mathbf{i} = \mathbf{k}$; $\mathbf{j}\mathbf{k} = -\mathbf{k}\mathbf{j} = \mathbf{i}$; $\mathbf{k}\mathbf{i} = -\mathbf{i}\mathbf{k} = \mathbf{j}$. In addition, if $e \in \mathbb{H}$, then we have $\bar{e} = e_0 - e_1\mathbf{i} - e_2\mathbf{j} - e_3\mathbf{k}$, and $\|e\| = \sqrt{e\bar{e}} = \sqrt{e_0^2 + e_1^2 + e_2^2 + e_3^2}$. The notion of quaternion is needed when we introduce the definition of the Fourier transform of a 2D signal by identifying the quaternion unit \mathbf{j} as the imaginary unit \mathbf{i} as well as the Riesz transform. The Fourier transform of a 2D signal $g(\mathbf{x}) \in L^2(\mathbb{R}^2)$ is given by

$$\mathcal{F}g(\boldsymbol{\xi}) = G(\boldsymbol{\xi}) := \int_{\mathbb{R}^2} g(\mathbf{x}) e^{-2\pi\mathbf{j}\boldsymbol{\xi}^T \mathbf{x}} d\mathbf{x}.$$

Let us define the *Riesz transform* [15, 13] of $g(\mathbf{x}) \in L^2(\mathbb{R}^2)$ by

$$\mathcal{R}g(\mathbf{x}) := \mathbf{i}\mathcal{R}_1g(\mathbf{x}) + \mathbf{j}\mathcal{R}_2g(\mathbf{x}), \quad \mathcal{R}_l g(\mathbf{x}) := (r_l * g)(\mathbf{x}), \quad l = 1, 2,$$

where $r_l(\mathbf{x}) := x_l / (2\pi\|\mathbf{x}\|^3)$ is the *Riesz kernel*. Note that the Fourier transform of the Riesz kernel $\mathcal{F}r_l(\boldsymbol{\xi}) = -\mathbf{j}\boldsymbol{\xi}_l / \|\boldsymbol{\xi}\|$ can be contrasted with that of the 1D Hilbert transform kernel: $\mathcal{F}h(\xi) = -\mathbf{i}\text{sgn}(\xi) = -\mathbf{i}\xi/|\xi|$ where $h(x) := 1/(\pi x)$. The monogenic signal g^+ of the signal g is now defined by introducing an operator $\mathcal{M}^+ := \mathbf{I} + \mathcal{R}$ [8, 9] such that

$$\mathcal{M}^+g(\mathbf{x}) = g^+(\mathbf{x}) := g(\mathbf{x}) + \mathcal{R}g(\mathbf{x}).$$

A monogenic signal can be decomposed into ‘‘instantaneous’’ amplitude, phase, and orientation components [9] as follows:

$$g^+(\mathbf{x}) = A(\mathbf{x}) (\cos \phi(\mathbf{x}) + \mathbf{v}(\mathbf{x}) \sin \phi(\mathbf{x})), \quad (1)$$

where $A(\mathbf{x}) := \|g^+(\mathbf{x})\|$, $\phi(\mathbf{x}) := \cos^{-1}(g(\mathbf{x})/\|g^+(\mathbf{x})\|)$, and $\mathbf{v}(\mathbf{x}) := \mathcal{R}g(\mathbf{x})/\|\mathcal{R}g(\mathbf{x})\|$ describe the *amplitude*, *phase*, and *phase direction (or orientation)* information locally at $\mathbf{x} \in \mathbb{R}^2$, respectively. Note that $\|\mathcal{R}g(\mathbf{x})\| := \sqrt{|g^{(1)}(\mathbf{x})|^2 + |g^{(2)}(\mathbf{x})|^2}$ whereas $\|g^+(\mathbf{x})\| := \sqrt{|g(\mathbf{x})|^2 + \|\mathcal{R}g(\mathbf{x})\|^2}$. Finally, the MWT is defined as the 2D CWT with a monogenic mother wavelet.

3. MONOGENIC WAVELET SCATTERING NETWORK

3.1. Basics of scattering transform network

Let Q_m be a discrete finite rotation group in \mathbb{R}^2 at layer m . Note that in any STN architecture, m is typically set at 2, i.e., it is quite shallow compared to DNNs. Denote $\Lambda_m := Q_m \times \mathbb{Z}$ the m -th layer index set consisting of the rotation $q \in Q_m$ and the scale $j \in \mathbb{Z}$. Let $\lambda_m = (q, j) \in \Lambda_m$ be the index for a multiscale directional wavelet filter at layer m . We can obtain such wavelet filters by dilating and rotating a mother wavelet ψ . The generator or the multiscale directional wavelet corresponds to the index $\lambda_m = (q, j)$ is

$$\psi_{\lambda_m}(\mathbf{x}) := 2^{2j}\psi(2^j q^{-1}\mathbf{x}).$$

Note that we assume the generator $\psi_{\lambda_m} \in L^1(\mathbb{R}^2) \cap L^2(\mathbb{R}^2)$. It is known as a frame atom and corresponds to a receptive field of a CNN [16].

To be more precise, let $f \in L^2(\mathbb{R}^2)$, and let us define a *translation* operator $T_{\mathbf{b}}f(\mathbf{x}) := f(\mathbf{x} - \mathbf{b})$ and an *involution* operator operator $I f(\mathbf{x}) := f(-\mathbf{x})$. Then, a *frame atom* is defined by $\psi_{\mathbf{b}, \lambda_m} := T_{\mathbf{b}}I\psi_{\lambda_m}$. Note that $\langle f, \psi_{\mathbf{b}, \lambda_m} \rangle = f * \psi_{\lambda_m}(\mathbf{b})$. A *contraction* operator M_m which is *Lipschitz continuous* can also be defined, and satisfies $M_m f(\mathbf{x}) = 0 \Rightarrow f(\mathbf{x}) = 0$. A particular choice of M_m is the *modulus* operator, i.e., $M_m f(\mathbf{x}) := |f(\mathbf{x})|$. We define an operator $U_m : \Lambda_m \times L^2(\mathbb{R}^2) \rightarrow L^2(\mathbb{R}^2)$ from layer $m-1$ to layer m such that

$$U_m[\lambda_m]f(\mathbf{x}) := M_m(f * \psi_{\lambda_m})(r_m \mathbf{x}). \quad (2)$$

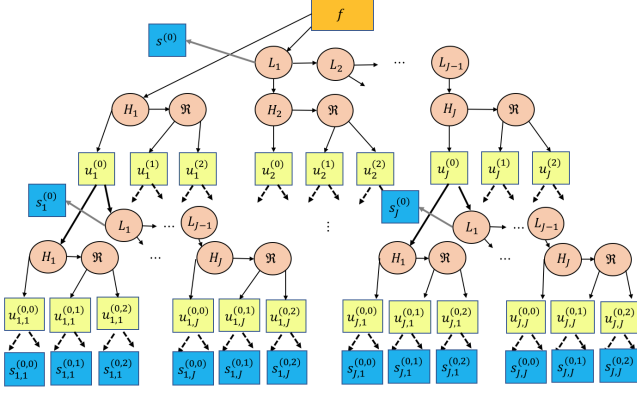


Fig. 1: The MWSN architecture

$r_m \geq 1$ represents a *subsampling rate*. Thus we have a *path* of indices $\lambda \in \Lambda_m \times \dots \times \Lambda_1$ such that

$$U[\lambda]f(\mathbf{x}) := U_m[\lambda_m]U_{m-1}[\lambda_{m-1}] \dots U_1[\lambda_1]f(\mathbf{x}). \quad (3)$$

For each layer m , we define the operators S_m and Φ_m to generate the output feature vectors (or coefficients) of the MWSN for a given input signal $f(\mathbf{x})$:

$$\begin{aligned} S_m[\lambda]f(\mathbf{x}) &:= (\varphi_m * U[\lambda]f)(r'_m \mathbf{x}), \\ \Phi_m f(\mathbf{x}) &:= \{S_m[\lambda]f(\mathbf{x})\}_{\lambda \in \Lambda_m \times \dots \times \Lambda_1}, \end{aligned} \quad (4)$$

where φ_m is an averaging function, e.g., the father wavelet of a certain scale corresponding to the mother wavelet ψ and $r'_m \geq 1$ provides yet another subsampling opportunity after this averaging process. Note that for $m = 0$, we set $S_0[\emptyset]f(\mathbf{x}) = S_0 f(\mathbf{x}) := (\varphi_0 * f)(r'_0 \mathbf{x})$.

3.2. Monogenic wavelet scattering network

The visual description of the Monogenic Wavelet Scattering Network (MWSN) is shown in Fig. 1. For the MWT implementation, we follow the strategy of Souillard and Carré [17] as follows. First, let us define a Gaussian high-pass filter H in the 2D Fourier domain:

$$H(\boldsymbol{\xi}) := 1 - e^{-\frac{\|\boldsymbol{\xi}\|^2}{2}}.$$

Then the Gaussian high-pass filter at scale j , denoted by H_j , is defined by

$$H_j(\boldsymbol{\xi}) := H(2^{j-1}\boldsymbol{\xi}), \quad j \in \{1, \dots, J\}, \quad (5)$$

where we typically use $J = 4$ in practice. A low-pass filter L_j at scale j can be defined as

$$L_j(\boldsymbol{\xi}) := \sqrt{1 - (H_j(\boldsymbol{\xi}))^2}.$$

In the MWSN framework, the MWT filter bank has intensive interaction with the feature from the previous layer. In

Fig. 1, the salmon-pink disks represent operators, i.e., H_j , L_j , and \mathcal{R} . Note that the convolution with the father wavelet φ_m at the m th layer in Eq. (4) in the conventional STN corresponds to the low-pass filtering with L_1 at every layer in the MWSN. The zeroth ($m = 0$) layer output is indicated by the blue box $S_0 f(\mathbf{x})$ ($\mathbf{s}^{(0)}$ for short) after the low-pass filtering with L_1 of the input image f followed by subsampling. The superscript (0) indicates the isotropic filtering is applied. In the first ($m = 1$) layer, the vectors $U_1[\lambda_1]f(\mathbf{x})$, $\lambda_1 \in \Lambda_1$ in the conventional STN of Eq. (2) is now denoted by the vectors in the yellow boxes, $\mathbf{u}_j^{(l)}$, $j \in \{1, \dots, J\}$, $l \in \{0, 1, 2\}$, where j is the scale parameter, and $l \in \{0, 1, 2\}$ indicates the isotropic component, the vertical and horizontal Riesz components obtained by \mathcal{R}_1 , \mathcal{R}_2 , respectively. The output vectors of the first layer, indicated by blue boxes such as $\mathbf{s}_1^{(0)}$ and $\mathbf{s}_j^{(0)}$, are obtained by subsampling $\mathbf{u}_j^{(l)}$, low-pass filtering with L_1 , and yet another subsampling. Note that the other first-layer outputs, i.e., $\mathbf{s}_j^{(0)}$, $j \in \{2, \dots, J-1\}$ and $\mathbf{s}_j^{(l)}$, $l \in \{1, 2\}$, $j \in \{1, \dots, J\}$ are omitted due to the crowded graphics. Now, in the second ($m = 2$) layer, the vector $U[\lambda]f(\mathbf{x}) = U[\lambda_2]U[\lambda_1]f(\mathbf{x})$ in the conventional STN of Eq. (3) is denoted by $\mathbf{u}_{j_1, j_2}^{(l_1, l_2)}$, $j_k \in \{1, \dots, J\}$, $l_k \in \{0, 1, 2\}$, $k = 1, 2$, where l_1, j_1 indicate the inherited first layer path information whereas l_2, j_2 are the parameters specified in the second layer. The outputs of the second layer are again obtained by applying the same procedure as the first layer to $\mathbf{u}_{j_1, j_2}^{(l_1, l_2)}$, which are indicated by blue boxes $\mathbf{s}_{j_1, j_2}^{(l_1, l_2)}$. Finally, the arrows in this diagram show the flow of the data; in addition, the thick arrows indicate that the subsampling operations are performed before reaching the destination disks or boxes while their color (gray or black) suggests that a potentially different subsampling rate can be set.

4. NUMERICAL RESULTS AND DISCUSSION

Using the CURET texture image dataset [18], we evaluated the classification performance of our MWSN and compared with that of the standard 2D STN based on Morlet wavelets [4, 5], i.e., the Kymatio package implemented by Andreux et al. [6] in the Python programming language. All the other codes we used for our experiments are based on the Julia programming language [19]. For each of 61 texture classes in the CURET dataset, we selected 92 texture images that were cropped to retain a 200×200 central region and converted to grayscale. Hence, the total number of available texture images is 5,612. We set the maximum scale parameter $J = 4$ in Eq. (5) in the MWSN, which exactly corresponds to $J = 3$ in the Kymatio package. For both methods, we only used the second layer outputs because they contain the most relevant information. The subsampling rates in the MWSN were set to 2 regardless of the layers while we used the default values in the Kymatio-STN. Since the Kymatio-STN allows the users to choose the number of orientations of the Morlet wavelets, we tried the number of ori-

Method	Dimension before PCA	Classification Accuracy
MWSN	90,000	97.34%
Kymatio-STN (L = 2)	11,875	94.50%
Kymatio-STN (L = 4)	38,125	96.18%
Kymatio-STN (L = 6)	79,375	96.56%
Kymatio-STN (L = 8)	135,625	96.61%

Table 1: Table of average test accuracy over 10 experiments

entations $L = 2, 4, 6, 8$. In each case, we used the PCA implemented in the `MultivariateStats.jl` package [20] to reduce the dimension of the coefficient/feature vectors of the MWSN and the Kymatio-STN. After some experiments, we decided to use the top 30 PCA coordinates for all cases. Then, those coordinates were fed to the Support Vector Machine (SVM) classifier (of a polynomial kernel of degree 1) implemented in the `LIBSVM.jl` package [21] that is based on the C++ library `LIBSVM` [22]. Table 1 lists the average test accuracy by repeating two-fold cross validation 10 times for each case along with the coefficient/feature vector dimension before the PCA was applied. The best accuracy achieved by our proposed MWSN is due to the natural extension of analyticity in 1D to monogenicity in 2D. The CWT with Morlet wavelets retain less properties than the MWT due to the “leak” of the energy to the negative frequency range. Together with the fact that the Riesz kernels are effective 2D edge detectors, fewer contextual directions in the MWSN can still capture sufficient textural information to achieve the better classification result than the Kymatio-STN does at least for this particular CURET texture image dataset.

The output coefficients of our proposed MWSN are also “interpretable.” Interpretability was rarely considered in the earlier studies on texture classification. Fig. 2b and Fig. 3 clearly illustrate the orientation information of an image captured by the Riesz transforms, \mathcal{R}_1 and \mathcal{R}_2 , respectively. In Fig. 3, the (i, j) th block contains 25×25 MWSN coefficients $\mathbf{s}_{j_1, j_2}^{(l_1, l_2)}$ with $l_1 = (i - 1) \bmod 3$, $l_2 = (j - 1) \bmod 3$, $j_1 = \lfloor (i - 1) / 3 \rfloor + 1$, and $j_2 = \lfloor (j - 1) / 3 \rfloor + 1$, where $i, j \in \{1, \dots, 12\}$. As we traverse from left to right at each row of Fig. 3, we see more intricate texture information is captured.

To improve the interpretability of the MWSN coefficients that are important for classification, we have three plans: 1) replace SVM by the logistic regression classifier [23, Chap. 3] so that we can pinpoint such MWSN coefficients; 2) convert the second layer coefficients $\mathbf{s}_{j_1, j_2}^{(l_1, l_2)}$ into the instantaneous amplitude, phase, and orientation representation via Eq. (1) before applying the PCA; and 3) replace the PCA by the Local Discriminant Basis (LDB) method [24, 25] since the latter can directly extract features that are helpful for classification instead of extracting high variance features by the PCA.

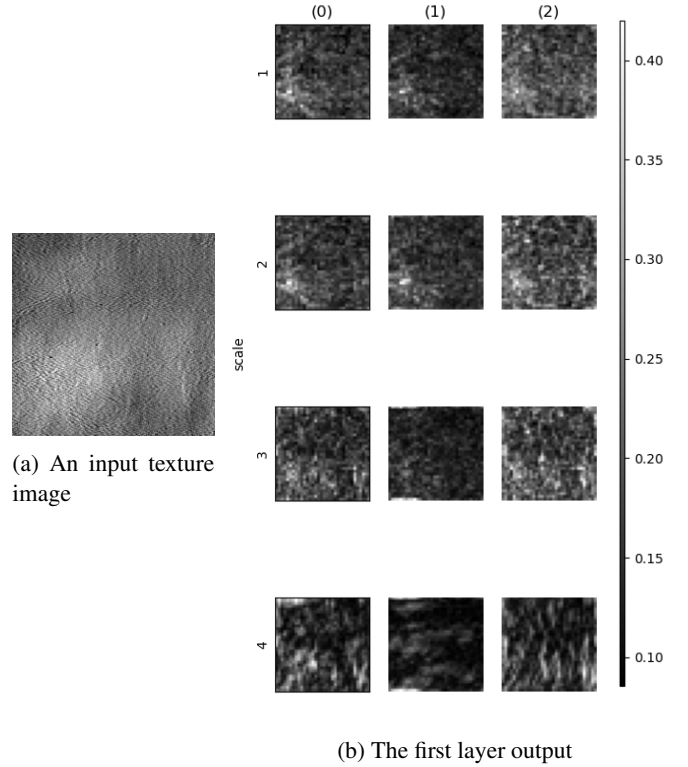


Fig. 2: A CURET image and its MWSN first layer output

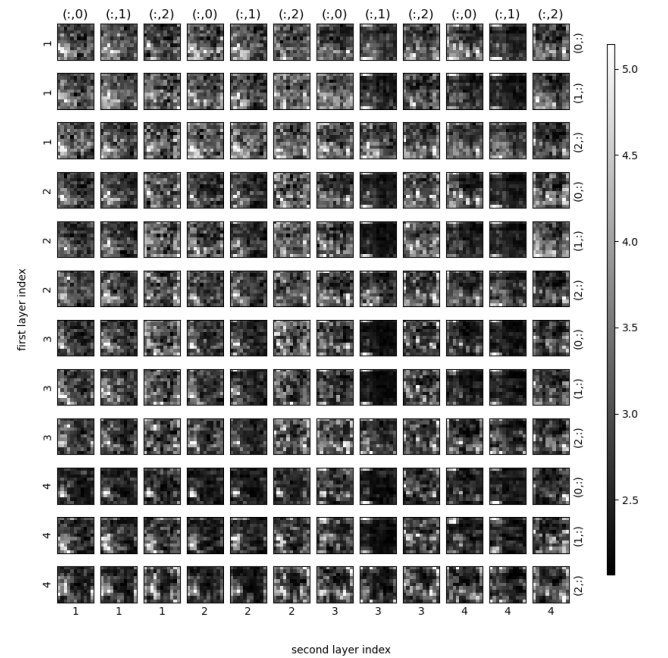


Fig. 3: The MWSN second layer output of the image shown in Fig. 2a

5. REFERENCES

- [1] Y. LeCun, Y. Bengio, and G. Hinton, “Deep learning,” *Nature*, vol. 521, no. 7553, pp. 436–444, 2015.
- [2] Y. Sun, X. Wang, and X. Tang, “Deep convolutional network cascade for facial point detection,” in *Proceedings of the IEEE Conference on Computer Vision and Pattern Recognition*, 2013, pp. 3476–3483.
- [3] S. Mallat, “Group invariant scattering,” *Communications on Pure and Applied Mathematics*, vol. 65, no. 10, pp. 1331–1398, 2012.
- [4] J. Bruna and S. Mallat, “Classification with scattering operators,” in *Proceedings of the IEEE Conference on Computer Vision and Pattern Recognition 2011*. IEEE, 2011, pp. 1561–1566.
- [5] J. Bruna and S. Mallat, “Invariant scattering convolution networks,” *IEEE Trans. Pattern Anal. Machine Intell.*, vol. 35, no. 8, pp. 1872–1886, 2013.
- [6] M. Andreux, T. Angles, G. Exarchakis, R. Leonarduzzi, G. Rochette, L. Thiry, J. Zarka, S. Mallat, J. Andén, E. Belilovsky, et al., “Kymatio: Scattering transforms in python,” *J. Mach. Learn. Res.*, vol. 21, no. 60, pp. 1–6, 2020.
- [7] J. M. Lilly and S. C. Olhede, “Higher-order properties of analytic wavelets,” *IEEE Trans. Signal Process.*, vol. 57, no. 1, pp. 146–160, 2009.
- [8] M. Felsberg and G. Sommer, “The monogenic signal,” *IEEE Trans. Signal Process.*, vol. 49, no. 12, pp. 3136–3144, 2001.
- [9] P. Cerejeiras and U. Kähler, “Monogenic signal theory,” in *Operator Theory*, D. Alpay, Ed. Springer, Basel, 2014, https://doi.org/10.1007/978-3-0348-0692-3_14-1.
- [10] S. C. Olhede and G. Metikas, “The monogenic wavelet transform,” *IEEE Trans. Signal Process.*, vol. 57, no. 9, pp. 3426–3441, 2009.
- [11] D. Gabor, “Theory of communication,” *J. IEE (London)*, vol. 93, pp. 429–457, 1946.
- [12] J. Ville, “Théorie et applications de la notion de signal analytique,” *Cables et Transmissions*, vol. 2ème A, no. 1, pp. 61–74, 1948.
- [13] S. L. Hahn, *Hilbert Transforms in Signal Processing*, Artech House Inc, Boston, London, 1996.
- [14] S. Mallat, *A Wavelet Tour of Signal Processing*, Academic Press, Burlington, MA, third edition, 2009.
- [15] E. M. Stein and G. Weiss, *Introduction to Fourier Analysis on Euclidean Spaces*, vol. 32 of *Princeton Mathematical Series*, Princeton Univ. Press, 1971.
- [16] T. Wiatowski and H. Bölcskei, “A mathematical theory of deep convolutional neural networks for feature extraction,” *IEEE Trans. Inform. Theory*, vol. 64, no. 3, pp. 1845–1866, 2018.
- [17] R. Souillard and P. Carré, “Characterization of color images with multiscale monogenic maxima,” *IEEE Trans. Pattern Anal. Machine Intell.*, vol. 40, no. 10, pp. 2289–2302, 2018.
- [18] K. J. Dana, B. Van Ginneken, S. K. Nayar, and J. J. Koenderink, “Reflectance and texture of real-world surfaces,” *ACM Transactions On Graphics (TOG)*, vol. 18, no. 1, pp. 1–34, 1999.
- [19] J. Bezanson, A. Edelman, S. Karpinski, and V. B. Shah, “Julia: A fresh approach to numerical computing,” *SIAM Review*, vol. 59, no. 1, pp. 65–98, 2017.
- [20] Julia Statistics, “MultivariateStats.jl: A Julia package for multivariate statistics and data analysis,” <https://github.com/JuliaStats/MultivariateStats.jl>, 2022.
- [21] S. Kornblith and M. Pastell, “LIBSVM.jl: A Julia interface for libsvm,” <https://github.com/JuliaML/LIBSVM.jl>, 2021.
- [22] C.-C. Chang and C.-J. Lin, “LIBSVM: A library for support vector machines,” *ACM Transactions on Intelligent Systems and Technology*, vol. 2, pp. 27:1–27:27, 2011, Software available at <http://www.csie.ntu.edu.tw/~cjlin/libsvm>.
- [23] T. Hastie, R. Tibshirani, and M. Wainwright, *Statistical Learning with Sparsity: The Lasso and Generalizations*, vol. 143 of *Monographs on Statistics and Applied Probability*, CRC Press, Boca Raton, FL, 2015.
- [24] N. Saito and R. R. Coifman, “Local discriminant bases and their applications,” *J. Math. Imaging Vis.*, vol. 5, no. 4, pp. 337–358, 1995, Invited paper.
- [25] N. Saito, R. R. Coifman, F. B. Geshwind, and F. Warner, “Discriminant feature extraction using empirical probability density estimation and a local basis library,” *Pattern Recognition*, vol. 35, no. 12, pp. 2841–2852, 2002.